Comparison of Prostate-Specific Membrane Antigen–Based 18F-DCFBC PET/CT to Conventional Imaging Modalities for Detection of Hormone-Naïve and Castration-Resistant Metastatic Prostate Cancer

Steven P. Rowe[1], **Katarzyna J. Macura**[1,2,3], **Anthony Ciarallo**[1], **Esther Mena**[1], **Amanda Blackford**[2], **Rosa Nadal**[2], **Emmanuel S. Antonarakis**[2], **Mario A. Eisenberger**[2], **Michael A. Carducci**[2], **Ashley E. Ross**[3], **Philip W. Kantoff**[4], **Daniel P. Holt**[1], **Robert F. Dannals**[1], **Ronnie C. Mease**[1], **Martin G. Pomper**[1], and **Steve Y. Cho**[1]

[1]The Russell H. Morgan Department of Radiology and Radiological Science, Johns Hopkins Medical Institutions, Baltimore, Maryland [2]Department of Medical Oncology, Johns Hopkins Medical Institutions, Baltimore, Maryland [3]The James Buchanan Brady Urological Institute and Department of Urology, Johns Hopkins Medical Institutions, Baltimore, Maryland [4]Dana Farber Cancer Institute, Harvard Medical School, Boston, Massachusetts

Abstract

Conventional imaging modalities (CIMs) have limited sensitivity and specificity for detection of metastatic prostate cancer. We examined the potential of a first-in-class radiofluorinated small-molecule inhibitor of prostate-specific membrane antigen (PSMA), *N*-[*N*-[(*S*)-1,3-dicarboxypropyl]carbamoyl]-4-^{18}F-fluorobenzyl-L-cysteine (^{18}F-DCFBC), to detect metastatic hormone-naïve (HNPC) and castration-resistant prostate cancer (CRPC).

Methods—Seventeen patients were prospectively enrolled (9 HNPC and 8 CRPC); 16 had CIM evidence of new or progressive metastatic prostate cancer and 1 had high clinical suspicion of metastatic disease. ^{18}F-DCFBC PET/CT imaging was obtained with 2 successive PET scans starting at 2 h after injection. Patients were imaged with CIM at approximately the time of PET. A lesion-by-lesion analysis of PET to CIM was performed in the context of either HNPC or CRPC. The patients were followed with available clinical imaging as a reference standard to determine the true nature of identified lesions on PET and CIM.

Results—On the lesion-by-lesion analysis, ^{18}F-DCFBC PET was able to detect a larger number of lesions (592 positive with 63 equivocal) than CIM (520 positive with 61 equivocal) overall, in both HNPC and CRPC patients. ^{18}F-DCFBC PET detection of lymph nodes, bone lesions, and visceral lesions was superior to CIM. When intrapatient clustering effects were considered, ^{18}F-DCFBC PET was estimated to be positive in a large proportion of lesions that would be negative or equivocal on CIM (0.45). On follow-up, the sensitivity of ^{18}F-DCFBC PET (0.92) was superior

---

to CIM (0.71). ^{18}F-DCFBC tumor uptake was increased at the later PET time point (∼2.5 h after injection), with background uptake showing a decreasing trend on later PET.

Conclusion—PET imaging with ^{18}F-DCFBC, a small-molecule PSMA-targeted radiotracer, detected more lesions than CIM and promises to diagnose and stage patients with metastatic prostate cancer more accurately than current imaging methods.

Keywords

Prostate cancer is common, representing the most frequent cancer diagnosis and second most frequent cause of cancer-related death in men in the United States (1). Many men who undergo curative therapy for primary prostate cancer will experience recurrent/metastatic disease. After a patient demonstrates biochemical recurrence, with newly appearing or increasing prostate-specific antigen blood levels, subsequent treatments such as androgen deprivation or cytotoxic chemotherapy are often deferred until there has been unequivocal new or progressive metastatic disease on imaging. That emphasizes the need for imaging of metastatic prostate cancer to be highly sensitive and specific to ensure that patients are treated appropriately in a timely manner.

Patients experiencing biochemical recurrence may be imaged with the conventional imaging modalities (CIMs) of ^{99m}Tc-methylene diphosphonate (MDP) bone scanning (BS) and contrast-enhanced CT (CECT) of the chest, abdomen, and pelvis. There are important limitations to the sensitivity and specificity of CIMs including small (<1 cm short axis) lymph nodes that are not definitively characterized as on CECT; primarily lytic bone lesions that may have little uptake on BS and be occult on CECT until significant trabecular or cortical destruction has occurred; and areas of degenerative bone change that are sclerotic on CECT and have high uptake on BS and that can be mistaken for, or obscure, osteoblastic osseous metastases.

Partly as a result of these limitations, there has been interest in the development of functional imaging tools for the detection of metastatic prostate cancer. ^{18}F-FDG PET/CT, despite widespread use in a variety of cancers, has generally proven to be problematic in this setting. An array of additional PET radiotracers has been investigated in metastatic prostate cancer including those targeting fatty acid metabolism (^{11}C-choline, ^{18}F-fluorocholine, and ^{11}C-acetate) (2–9) and amino acid transport (anti-1-amino-3-^{18}F-fluorocyclobutane-1-carboxylic acid) (10–12). Additional radiotracers targeting the prostate-specific membrane antigen (PSMA) include small-molecule (13–18) and antibody (19–21) agents. Gastrin-releasing peptide (22) and glutamine-(23,24) targeted radiotracers are also being developed.

PSMA is an attractive target for imaging prostate cancer because it is expressed in most prostate cancers and histologic studies have associated high PSMA expression with metastatic spread (25,26) and castration resistance (27–29), and expression levels may be predictive of progression (30,31). Our previous work has shown that a radiofluorinated small-molecule inhibitor of PSMA, N-[N-[(S)-1,3-dicarboxypropyl]carbamoyl]-4-[18]F-

fluorobenzyl-ʟ-cysteine (^{18}F-DCFBC; Fig. 1), was able to concentrate in PSMA-expressing tumors in preclinical studies (14), to identify sites of metastatic disease clinically (13), and to localize at sites of high-grade primary prostate cancer (32). For this study, we evaluated the ability of ^{18}F-DCFBC PET/CT to identify sites of bone, lymph node, and visceral soft-tissue metastatic disease in comparison to CIM. The study cohort consisted of both hormone-naïve and castration-resistant metastatic prostate cancer patients.

Materials and Methods

Patient Population and Selection

Our hospital's Institutional Review Board approved this study under the auspices of a Food and Drug Administration exploratory investigation new drug application (eIND 108943). This clinical trial was registered in ClinicalTrials.gov (identifier NCT01815515). Written, informed consent was obtained from all participating patients. Inclusion criteria for this study included histologic confirmation of prostate cancer, radiologic evidence of new or progressive metastatic disease on anatomic or functional imaging, and rising prostate-specific antigen serum levels on 2 observations at least 1 wk apart. Exclusion criteria included the patient being treated with an investigational drug, biologic, or device within 14 d of ^{18}F-DCFBC administration; initiation of new prostate cancer therapy within 14 d of ^{18}F-DCFBC administration; initiation of new therapy for progressive metastatic disease since radiographic documentation of progression; serum creatinine or total bilirubin greater than 3 times the upper limit of normal; or liver transaminases greater than 5 times the upper limit of normal. These baseline laboratory values were obtained to ensure patients were appropriately healthy enough to reasonably participate in the study. Patients underwent CECT of the chest, abdomen, and pelvis (single, venous phase) and planar BS within 28 d of ^{18}F-DCFBC PET.

Seventeen patients were prospectively enrolled and imaged with ^{18}F-DCFBC PET/CT between May 2013 and May 2014. Patients were followed up to 1 y with subsequent imaging examinations obtained at the discretion of the treating medical oncologists.

Radiochemistry

2-[3-(1-carboxy-2-mercapto-ethyl)-ureido]-pentanedioic acid was synthesized as previously detailed (33). Nonradioactive DCFBC was prepared according to a modification of a published protocol with conformation to current good manufacturing practice (14). ^{18}F-DCFBC (radiolabeled) was prepared according to published protocols (13,34). Specific activity range of administered ^{18}F-DCFBC was 697 ± 263 GBq/μmol ($18,837 \pm 7,095$ mCi/μmol).

PET/CT Protocol

Patients were instructed to take nothing by mouth (except for water and some medications) for at least 6 h before the administration of ^{18}F-DCFBC. Because other investigators have noted the ability of folate to act as a substrate for PSMA (35–37), we asked that patients not take multivitamins or folate supplements on the day of ^{18}F-DCFBC PET/CT imaging. Blood was drawn and sent for serum folate, red blood cell folate, and testosterone levels (Table 1).

^{18}F-DCFBC PET/CT images were acquired on a Discovery DRX PET/CT scanner (GE Healthcare) operating in 3-dimensional emission mode with CT-derived attenuation correction. A bolus injection of 370 ± 37 MBq (10 ± 1 mCi) of ^{18}F-DCFBC was administered intravenously. Two hours after injection, a whole-body (WB; from the top of the skull through the mid thighs) CT was obtained (120 kVp, 80 mA maximum [auto-adjusting]) followed by an initial WB PET acquisition beginning at the mid thighs with 4 min and 15 s per bed position (early time point). Given our earlier experience with ^{18}F-DCFBC from the first-in-human study, we suspected that imaging at a later time point after radiotracer injection might yield improved tumor uptake and decreased background. Accordingly, immediately after the initial PET acquisition, a second WB acquisition was obtained, again starting from the mid thighs and occurring approximately 2.5 h after injection (late time point). PET images were reconstructed using a clinical ordered-subset expectation maximization algorithm.

Image Analysis

^{18}F-DCFBC PET/CT and BS images were centrally reviewed by 3 expert nuclear medicine interpreters who reached a group consensus on the lesions for each scan. Analyses of the PET/CT and BS images on any 1 patient were performed at least 1 wk apart to minimize any bias that might occur in the interpretation of either the PET/CT or the BS based on results from the other study; although the number of patients was relatively small, a large number of lesions were identified, decreasing the likelihood that individual lesions would be recalled and mentally correlated by the central reviewers. CECT images were centrally reviewed by 2 expert interpreters who were masked to the results of the PET and BS studies and who also reached a group consensus read on each scan.

Visual analysis of ^{18}F-DCFBC uptake on the PET/CT scans was performed on a 3-point scale (1, negative/below adjacent background; 2, equivocal/approximately at adjacent background; and 3, positive/ above adjacent background) on both the early and the late time points on an Advantage Workstation (GE Healthcare). Maximum standardized uptake values (SUV_{max}) corrected for lean body mass were obtained from both time points. For lesions identified on other modalities that lacked discrete ^{18}F-DCFBC uptake, regions of interest were drawn at corresponding sites on the PET images to derive SUV_{max} levels for these lesions. One patient had diffusely infiltrating, biopsy-proven liver metastases that was interpreted as such by central review of the CECT and was negative (and hence not identified) on ^{18}F-DCFBC PET; this patient's liver was considered a single lesion for the purposes of analysis and SUV_{max} was determined from the most confluent focus of disease in the liver. To measure background, average SUVs were obtained from ascending aorta blood-pool activity, liver parenchyma in the non– disease-involved right lobe of the liver, within a vertebral body not involved with disease, and within the right gluteal muscles.

The BS and CECT images were analyzed on our institution's standard clinical viewing software, UltraVisual (Emageon). For both modalities, lesions were again classified on a 3-point scale. For lymph nodes on the CECT scans, a short-axis measurement less than 1 cm was considered negative and a short-axis measurement greater than 1 cm was considered positive.

During follow-up of these patients, any available imaging was reviewed by the appropriate central reviewers. Those lesions that demonstrated subjectively determined progression or response to therapy on the follow-up studies were considered to be true-positive lesions for the purposes of calculating sensitivity. Lesions that remained unchanged were considered equivocal, and sensitivity was calculated with these equivocal lesions grouped with either the positive or the negative lesions in separate analyses. One patient entered hospice and subsequently died of his metastatic disease after being imaged with ^{18}F-DCFBC PET but before any imaging follow-up could be completed; the nature of his lesions was established in consultation between the central imaging reviewers and medical oncologists.

Statistical Analysis

Each lesion was classified as positive, negative, or equivocal by ^{18}F-DCFBC PET/CT, CECT, BS, and combined CIM. The proportion of agreement between modalities was estimated using intercept-only logistic regression models with a generalized estimating equation (GEE) approach to account for intrapatient correlation of multiple lesions. In addition to an overall modality-based analysis, the proportion of agreement was also estimated for lesions based on location (i.e., lymph node, bone, or visceral soft tissue) as well as patient castrate status (hormone-naïve vs. resistant). Sensitivity was calculated on the basis of follow-up imaging findings using the GEE intercept-only approach described above. Differences in continuously measured parameters including SUV_{max} were estimated with linear regression models using GEE. Analyses were completed with R version 3.1.2 (https://cran.r-project.org/bin/windows/base/old/3.1.2/) (38).

Results

Study Population Baseline Imaging

Sixteen of 17 patients met all inclusion criteria; 1 patient lacked definite evidence of new or progressive metastatic disease on imaging, but there was a strong clinical suspicion that he would have detectable disease with ^{18}F-DCFBC PET, and the Institutional Review Board granted an exemption. Selected clinical and demographic data for the 17 imaged patients are included in Table 1. Of the 17 patients imaged with ^{18}F-DCFBC PET/CT, complete contemporaneous CIM (both CECT of the chest, abdomen, and pelvis and planar WB BS) was available for all but 3 patients. One patient had a history of severe allergy to iodinated contrast and was imaged with a noncontrast CT. A second patient underwent a follow-up CECT at an outside institution, but we were not able to obtain this scan for central review. The third patient underwent outside BS, but the images provided could not be obtained in DICOM format for adequate interpretation.

Imaging Findings

In aggregate, between ^{18}F-DCFBC PET and CIM, 714 metastatic lesions were detected on at least 1 modality (per patient: median, 17 lesions; range, 4–237 lesions). Positive ^{18}F-DCFBC PET uptake was observed visually in 592 lesions, with 63 additional lesions deemed equivocal. Overall, for diagnostic CT, 402 lesions were determined to be positive, with an additional 41 determined to be equivocal. For BS, 303 lesions were positive and 29

were equivocal. In total, 520 lesions were positive with CIM, with a further 61 equivocal lesions.

As shown in Figure 2A, the median and range of SUV_{max} for ^{18}F-DCFBC–positive metastatic lesions demonstrated higher uptake at the later time point ($P < 0.001$). The measured background PET average SUV trended lower on the later PET time point, though again it was not statistically significant (Fig. 2B). When ^{18}F-DCFBC PET–positive metastatic lesions in patients with HNPC and CRPC were compared, we did not observe a statistically significant difference in PET SUV_{max} in the lesions from the 2 patient populations ($P = 0.81$ for the early time point and 0.57 for the late time point). There was no difference in visual detection of metastatic lesions on early- and later-time-point PET acquisitions; thus, lesion positive/negative/equivocal status between the 2 acquisitions was unchanged for all detected lesions.

Statistical Analysis

The general estimating equation estimates for lesion detection by modality are detailed in Table 2 (the actual number of discrete lesions seen on each modality are included in Supplemental Table 1; supplemental materials are available at http:// jnm.snmjournals.org). ^{18}F-DCFBC PET was able to identify more definitive lesions than CIM. The estimated proportion of all detected metastatic lesions that would be positive with ^{18}F-DCFBC PET but negative or equivocal with CIM was 0.44 (95% confidence interval [CI], 0.28–0.61). The estimated proportion of lesions that would be positive on CIM but negative or equivocal on ^{18}F-DCFBC PET was 0.08 (95% CI, 0.04– 0.16). The estimated proportions for different types of metastatic sites are detailed in Table 2.

Despite the concern that high folate levels (defined in our hospital laboratory as >24 ng/mL serum folate) could potentially interfere with ^{18}F-DCFBC uptake in cells expressing PSMA, the range of number of lesions detected in patients with high folate was similar to the range in patients with normal folate levels (range, 16–172 in patients with high folate vs. 4–237 in patients with normal folate) with a higher median number of lesions in patients with high folate (47 in patients with high folate vs. 13.5 in patients with normal folate).

Of the original 17 patients recruited, 12 had adequate imaging follow-up to assess for progression, response, or stability of the lesions originally identified. This follow-up was generally with conventional imaging only, although a single patient did undergo a follow-up research PET scan with a PSMA-targeted radiotracer. Central review of the follow-up imaging was performed with individual lesions subjectively determined as progressing/ responding to therapy (true lesions) or remaining unchanged (equivocal). Table 3 details the available imaging and time to follow-up for each patient as well as the intercurrent therapy each received. Maximum time to follow-up was 1 y (median time to follow-up was 4 mo, with range from 1 mo to 1 y). The estimates for sensitivity of ^{18}F-DCFBC PET for true metastatic lesions, with equivocal lesions considered negative for metastasis, was 0.92 (95% CI, 0.80–0.97) as compared with a sensitivity of 0.64 (95% CI, 0.41–0.82) for CECT, 0.40 (95% CI, 0.20–0.65) for BS, and 0.71 (95% CI, 0.49–0.86) for combined CIM (Table 4).

Pertinent examples of imaging findings with ^{18}F-DCFBC are shown in Figures 3–6 and Supplemental Figure 1, as detailed in the accompanying figure legends.

Discussion

Significant progress has been made in the development of PET radiotracers for molecular imaging of metastatic prostate cancer, many of which have demonstrated promise for improving detection relative to CIM. We have presented prospective, systematic evidence of the superior sensitivity of the small-molecule PSMA inhibitor ^{18}F-DCFBC for detecting lesions in metastatic prostate cancer patients.

Of particular importance, patients with either HNPC or CRPC were reliably imaged with ^{18}F-DCFBC PET with no statistically significant difference in the observed SUV_{max} ranges for metastatic lesions. Given previously published data that had suggested increased PSMA expression with low androgen signaling, it was of concern that lesions in CRPC patients might have shown low uptake of a PSMA-targeted radiotracer. Recent clinical data from ^{68}Ga-labeled PSMA PET radiotracers have also demonstrated that metastatic lesions in CRPC express enough PSMA to be reliably detected (15,16).

^{18}F-DCFBC PET was capable of showing definitive focal radio-tracer uptake at sites of involvement that are often problematic in the interpretation of conventional imaging. Sclerotic lesions in the spine on CECT with corresponding ^{99m}Tc-MDP uptake on BS may be interpreted as indeterminate for metastatic involvement versus degenerative change (Fig. 3). Predominantly lytic or mixed bone lesions that can be subtle or are not visualized on CIM can also be well visualized on ^{18}F-DCFBC PET (Fig. 4). Furthermore, lymph node metastases that are too small to definitively identify with CIM can show focal ^{18}F-DCFBC uptake (Fig. 5).

Analysis of uptake at the early versus late time points suggests that the late time point produced both improved tumor uptake and decreased background distribution of ^{18}F-DCFBC. It is possible that even later imaging may further improve image quality, although the relatively high degree of activity within the blood pool for ^{18}F-DCFBC is likely to persist to at least some degree. The late time point in this study ($\sim$2.5–3 h after injection) is likely to represent a suitable compromise between optimizing image quality while preserving reasonable clinical workflow.

Potential limitations of ^{18}F-DCFBC PET/CT became apparent over the course of this study. A small number of densely sclerotic bone lesions were much more apparent on CIM (Fig. 6). Although the dense sclerosis and high ^{99m}Tc-MDP uptake are indicative of significant bony reaction to the presence of tumor cells, it may be that these lesions have relatively few metastatic prostate cancer cells and therefore a diminished ability to sequester PSMA-targeted radiotracers. A second potential pitfall we observed with ^{18}F-DCFBC was in the context of liver metastases, which were not well seen (Supplemental Fig. 1). The reason for this was not immediately apparent, although we suspect that although metastases are PSMA-avid, signal from such lesions is overwhelmed by background.

At the initiation of the study, a few patients could not or did not receive complete baseline CIM, preventing the most complete possible analysis. An additional significant limitation of this study was the lack of histopathologic truth standard; although we have attempted to mitigate this using the surrogate of response to therapy/ disease progression on follow-up imaging to assess for true lesions, this approach remains limited in that lesions identified on ^{18}F-DCFBC PET imaging were necessarily compared with follow-up conventional imaging. BS imaging in this study was only planar and tomographic bone scintigraphy or Na^{18}F PET would likely have detected more bone lesions, potentially narrowing the sensitivity difference between ^{18}F-DCFBC PET and CIM.

We recently conducted an initial clinical study with a second-generation ^{18}F-labeled PSMA ligand,2-(3-(1-carboxy-5-[(6-^{18}F-fluoro-pyridine-3-carbonyl)-amino]-pentyl)-ureido)-pentanedioic acid (DCFPyL), a chemical and mechanistic compound similar to ^{18}F-DCFBC but with higher binding affinity for PSMA and lower activity within the blood pool (39). We expect DCFPyL, as well as additional refinements to other PSMA-binding radiotracers, to address some of the limitations we have observed. There have been promising results as well for ^{68}Ga-PSMA radiotracers (15,16), with advantages being easier radiochemistry inherent in a generator-produced ^{68}Ga without need for a cyclotron and potential integration to theranostic applications. We favor the use of ^{18}F-PSMA agents, however, because of the ease of distribution using preexisting networks for ^{18}F-FDG and improved spatial resolution and more accurate quantitation inherent in the shorter positron range and higher positron yield of ^{18}F versus ^{68}Ga (40). Nonetheless, the systematic prospective evaluation of ^{18}F-DCFBC presented here indicates the promise of PET imaging of PSMA in general as a means to improve detection of metastatic prostate cancer.

Conclusion

PSMA-based PET/CT imaging with ^{18}F-DCFBC can detect more metastatic prostate cancer lesions than the current standard of clinical imaging with CECT and BS in patients with either HNPC or CRPC. PSMA-targeted imaging offers promise in more accurate identification of the presence and extent of metastatic prostate cancer.

Supplementary Material

Refer to Web version on PubMed Central for supplementary material.

Acknowledgments

References

1. Siegel R, Ma J, Zou Z, Jemal A. Cancer statistics, 2014. CA Cancer J Clin. 2014; 64:9–29. [PubMed: 24399786]

2. Bauman G, Belhocine T, Kovacs M, Ward A, Beheshti M, Rachinsky I. ^{18}F-fluorocholine for prostate cancer imaging: a systematic review of the literature. Prostate Cancer Prostatic Dis. 2012; 15:45–55. [PubMed: 21844889]

3. Beheshti M, Treglia G, Zakavi SR, et al. Application of ^{11}C-acetate positron-emission tomography (PET) imaging in prostate cancer: systematic review and meta-analysis of the literature. BJU Int. 2013; 2013:13.

4. Evangelista L, Guttilla A, Zattoni F, Muzzio PC. Utility of choline positron emission tomography/ computed tomography for lymph node involvement identification in intermediate- to high-risk prostate cancer: a systematic literature review and meta-analysis. Eur Urol. 2013; 63:1040–1048. [PubMed: 23036576]

5. Evangelista L, Zattoni F, Guttilla A, Saladini G, Colletti PM, Rubello D. Choline PET or PET/CT and biochemical relapse of prostate cancer: a systematic review and meta-analysis. Clin Nucl Med. 2013; 38:305–314. [PubMed: 23486334]

6. Fuccio C, Rubello D, Castellucci P, Marzola MC, Fanti S. Choline PET/CT for prostate cancer: main clinical applications. Eur J Radiol. 2011; 80:e50–e56. [PubMed: 20800404]

7. Jadvar H. Prostate cancer: PET with ^{18}F-FDG, [18]F- or ^{11}C-acetate, and [18]F- or ^{11}C-choline. J Nucl Med. 2011; 52:81–89. [PubMed: 21149473]

8. Mertens K, Slaets D, Lambert B, Acou M, De Vos F, Goethals I. PET with ^{18}F-labelled choline-based tracers for tumour imaging: a review of the literature. Eur J Nucl Med Mol Imaging. 2010; 37:2188–2193. [PubMed: 20544193]

9. Umbehr MH, Muntener M, Hany T, Sulser T, Bachmann LM. The role of ^{11}C-choline and ^{18}F-fluorocholine positron emission tomography (PET) and PET/CT in prostate cancer: a systematic review and meta-analysis. Eur Urol. 2013; 64:106–117. [PubMed: 23628493]

10. Schuster DM, Votaw JR, Nieh PT, et al. Initial experience with the radiotracer anti-1-amino-3-^{18}F-fluorocyclobutane-1-carboxylic acid with PET/CT in prostate carcinoma. J Nucl Med. 2007; 48:56–63. [PubMed: 17204699]

11. Schuster DM, Savir-Baruch B, Nieh PT, et al. Detection of recurrent prostate carcinoma with anti-1-amino-3-^{18}F-fluorocyclobutane-1-carboxylic acid PET/ CT and ^{111}In-capromab pendetide SPECT/CT. Radiology. 2011; 259:852–861. [PubMed: 21493787]

12. Mena E, Turkbey B, Mani H, et al. ^{11}C-acetate PET/CT in localized prostate cancer: a study with MRI and histopathologic correlation. J Nucl Med. 2012; 53:538–545. [PubMed: 22343504]

13. Cho SY, Gage KL, Mease RC, et al. Biodistribution, tumor detection, and radiation dosimetry of ^{18}F-DCFBC, a low-molecular-weight inhibitor of prostate-specific membrane antigen, in patients with metastatic prostate cancer. J Nucl Med. 2012; 53:1883–1891. [PubMed: 23203246]

14. Mease RC, Dusich CL, Foss CA, et al. N-[N-[(S)-1,3-dicarboxypropyl]carbamoyl]-4-[^{18}F]fluorobenzyl-l-cysteine, [^{18}F]DCFBC: a new imaging probe for prostate cancer. Clin Cancer Res. 2008; 14:3036–3043. [PubMed: 18483369]

15. Afshar-Oromieh A, Malcher A, Eder M, et al. PET imaging with a [^{68}Ga]gallium-labelled PSMA ligand for the diagnosis of prostate cancer: biodistribution in humans and first evaluation of tumour lesions. Eur J Nucl Med Mol Imaging. 2013; 40:486–495. [PubMed: 23179945]

16. Afshar-Oromieh A, Avtzi E, Giesel FL, et al. The diagnostic value of PET/CT imaging with the ^{68}Ga-labelled PSMA ligand HBED-CC in the diagnosis of recurrent prostate cancer. Eur J Nucl Med Mol Imaging. 2015; 42:197–209. [PubMed: 25411132]

17. Barrett JA, Coleman RE, Goldsmith SJ, et al. First-in-man evaluation of 2 high-affinity PSMA-avid small molecules for imaging prostate cancer. J Nucl Med. 2013; 54:380–387. [PubMed: 23303962]

18. Vallabhajosula S, Nikolopoulou A, Babich JW, et al. ^{99m}Tc-labeled small-molecule inhibitors of prostate-specific membrane antigen: pharmacokinetics and biodistribution studies in healthy subjects and patients with metastatic prostate cancer. J Nucl Med. 2014; 55:1791–1798. [PubMed: 25342385]

19. Tagawa ST, Milowsky MI, Morris M, et al. Phase II study of lutetium-177-labeled anti-prostate-specific membrane antigen monoclonal antibody J591 for metastatic castration-resistant prostate cancer. Clin Cancer Res. 2013; 19:5182–5191. [PubMed: 23714732]

20. Viola-Villegas NT, Sevak KK, Carlin SD, et al. Noninvasive imaging of PSMA in prostate tumors with [89]Zr-labeled huJ591 engineered antibody fragments: the faster alternatives. Mol Pharm. 2014; 11:3965–3973. [PubMed: 24779727]

21. Osborne JR, Green DA, Spratt DE, et al. A prospective pilot study of [89]Zr-J591/ prostate specific membrane antigen positron emission tomography in men with localized prostate cancer undergoing radical prostatectomy. J Urol. 2014; 191:1439–1445. [PubMed: 24135437]

22. Wieser G, Mansi R, Grosu AL, et al. Positron emission tomography (PET) imaging of prostate cancer with a gastrin releasing peptide receptor antagonist– from mice to men. Theranostics. 2014; 4:412–419. [PubMed: 24578724]

23. Lieberman BP, Ploessl K, Wang L, et al. PET imaging of glutaminolysis in tumors by [18]F-(2S, 4R)4-fluoroglutamine. J Nucl Med. 2011; 52:1947–1955. [PubMed: 22095958]

24. Venneti S, Dunphy MP, Zhang H, et al. Glutamine-based PET imaging facilitates enhanced metabolic evaluation of gliomas in vivo. Sci Transl Med. 2015; 7:274ra17.

25. Sweat SD, Pacelli A, Murphy GP, Bostwick DG. Prostate-specific membrane antigen expression is greatest in prostate adenocarcinoma and lymph node metastases. Urology. 1998; 52:637–640. [PubMed: 9763084]

26. Chang SS, Reuter VE, Heston WD, Gaudin PB. Comparison of anti-prostate-specific membrane antigen antibodies and other immunomarkers in metastatic prostate carcinoma. Urology. 2001; 57:1179–1183. [PubMed: 11377343]

27. Wright GL Jr, Grob BM, Haley C, et al. Upregulation of prostate-specific membrane antigen after androgen-deprivation therapy. Urology. 1996; 48:326–334. [PubMed: 8753752]

28. Evans MJ, Smith-Jones PM, Wongvipat J, et al. Noninvasive measurement of androgen receptor signaling with a positron-emitting radiopharmaceutical that targets prostate-specific membrane antigen. Proc Natl Acad Sci USA. 2011; 108:9578–9582. [PubMed: 21606347]

29. Noss KR, Wolfe SA, Grimes SR. Upregulation of prostate specific membrane antigen/folate hydrolase transcription by an enhancer. Gene. 2002; 285:247–256. [PubMed: 12039052]

30. Perner S, Hofer MD, Kim R, et al. Prostate-specific membrane antigen expression as a predictor of prostate cancer progression. Hum Pathol. 2007; 38:696–701. [PubMed: 17320151]

31. Ross JS, Sheehan CE, Fisher HA, et al. Correlation of primary tumor prostate-specific membrane antigen expression with disease recurrence in prostate cancer. Clin Cancer Res. 2003; 9:6357–6362. [PubMed: 14695135]

32. Rowe SP, Gage KL, Faraj SF, et al. ^{18}F-DCFBC PET/CT for PSMA-based detection and characterization of primary prostate cancer. J Nucl Med. 2015; 56:1003–1010. [PubMed: 26069305]

33. Kozikowski AP, Nan F, Conti P, et al. Design of remarkably simple, yet potent urea-based inhibitors of glutamate carboxypeptidase II (NAALADase). J Med Chem. 2001; 44:298–301. [PubMed: 11462970]

34. Holt DPRH, Mathews WB, Horti A, Mease R, Dannals RF. A semi-automated microwave chemistry system for complete radiosynthesis, purification, and formulation of F-18 radiotracers. J Label Compd Radiopharm. 2011; 54

35. Foss CA, Mease RC, Cho SY, Kim HJ, Pomper MG. GCPII imaging and cancer. Curr Med Chem. 2012; 19:1346–1359. [PubMed: 22304713]

36. Yao V, Berkman CE, Choi JK, O'Keefe DS, Bacich DJ. Expression of prostate-specific membrane antigen (PSMA), increases cell folate uptake and proliferation and suggests a novel role for PSMA in the uptake of the non-polyglutamated folate, folic acid. Prostate. 2010; 70:305–316. [PubMed: 19830782]

37. Yao V, Parwani A, Maier C, Heston WD, Bacich DJ. Moderate expression of prostate-specific membrane antigen, a tissue differentiation antigen and folate hydrolase, facilitates prostate carcinogenesis. Cancer Res. 2008; 68:9070–9077. [PubMed: 18974153]

38. The R Foundation. [Accessed November 10, 2015] R: A Language and Environment for Statistical Computing. The R Foundation website. https://www.r-project.org/. Updated August 2015

39. Szabo Z, Mena E, Rowe SP, et al. Initial evaluation of [F]DCFPyL for prostate-Specific membrane antigen (PSMA)-targeted PET imaging of prostate cancer. Mol Imaging Biol. 2015; 17:565–574. [PubMed: 25896814]
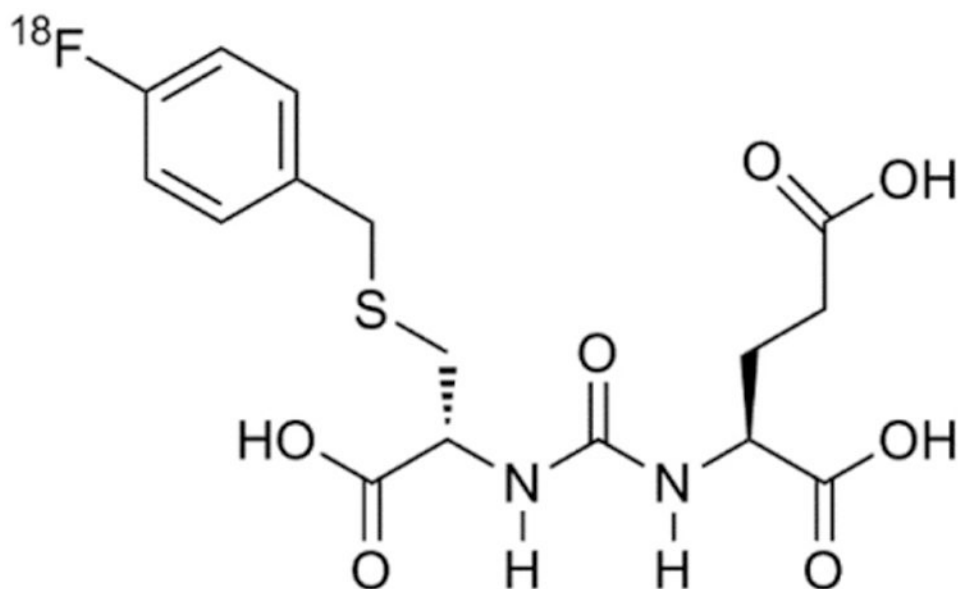
40. Sanchez-Crespo A. Comparison of gallium-68 and fluorine-18 imaging characteristics in positron emission tomography. Appl Radiat Isot. 2013; 76:55–62. [PubMed: 23063597]

Figure 1.
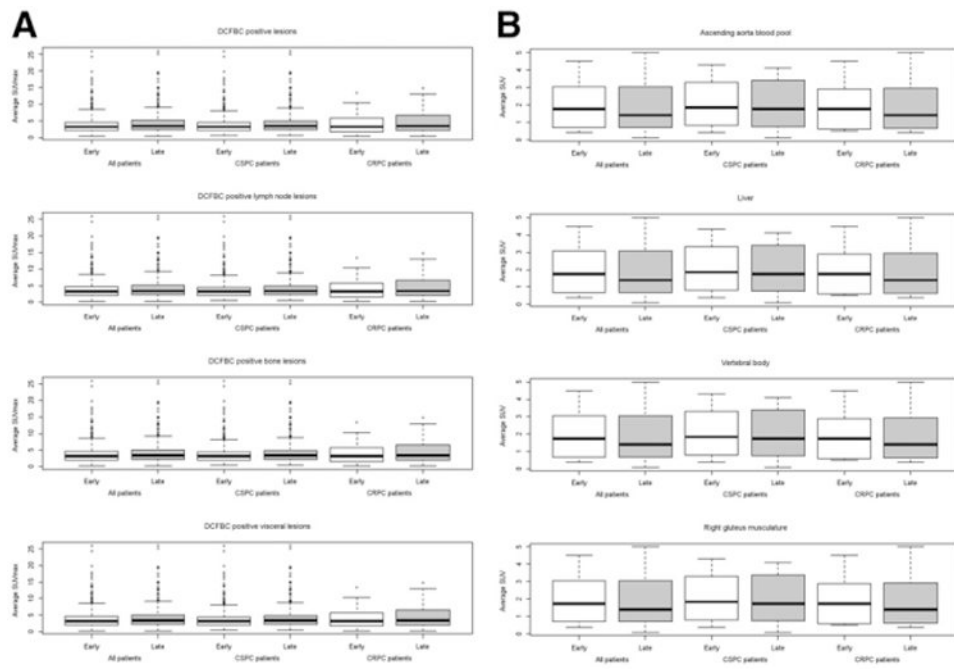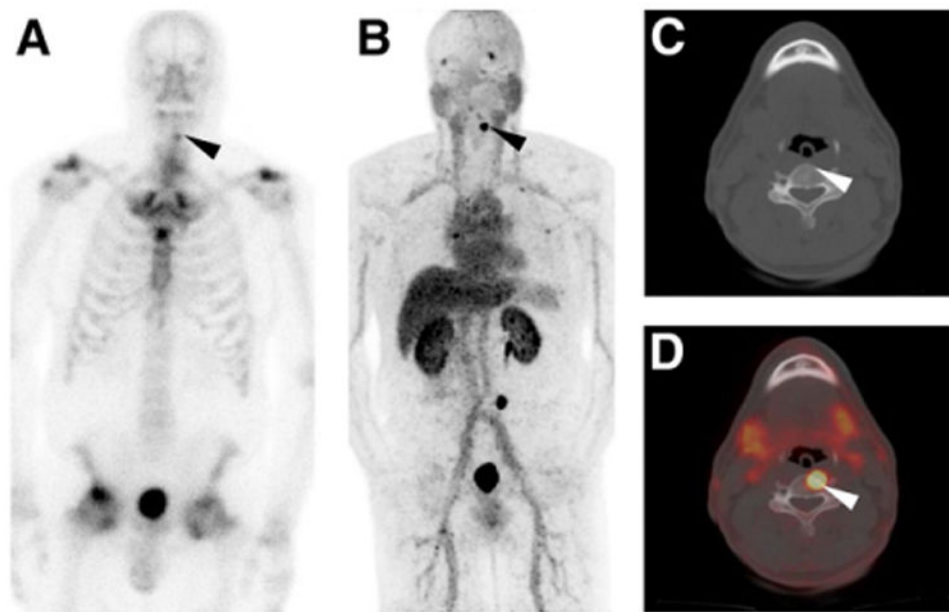Chemical structure of ^{18}F-DCBFC, first-in-class radiofluorinated inhibitor of PSMA.

Figure 2.
Box plot of SUV_{max} for ^{18}F-DCFBC PET–positive metastatic lesions by location and patient's androgen-resistant status (A) and box plot of average SUV for various regions of background physiologic uptake (B).

Figure 3.
Anterior projection planar BS (A), ^{18}F-DCFBC PET maximum-intensity projection (B), axial CT (C), and axial ^{18}F-DCFBC PET/CT fusion (D) images from patient thought to have degenerative arthritic changes at site of ^{99m}Tc-MDP uptake on bone scan (black arrowhead in A). However, intense focal ^{18}F-DCFBC uptake was also noted at this site that progressed on follow-up corresponding to rise in prostate-specific antigen (black and white arrowheads in B–D).
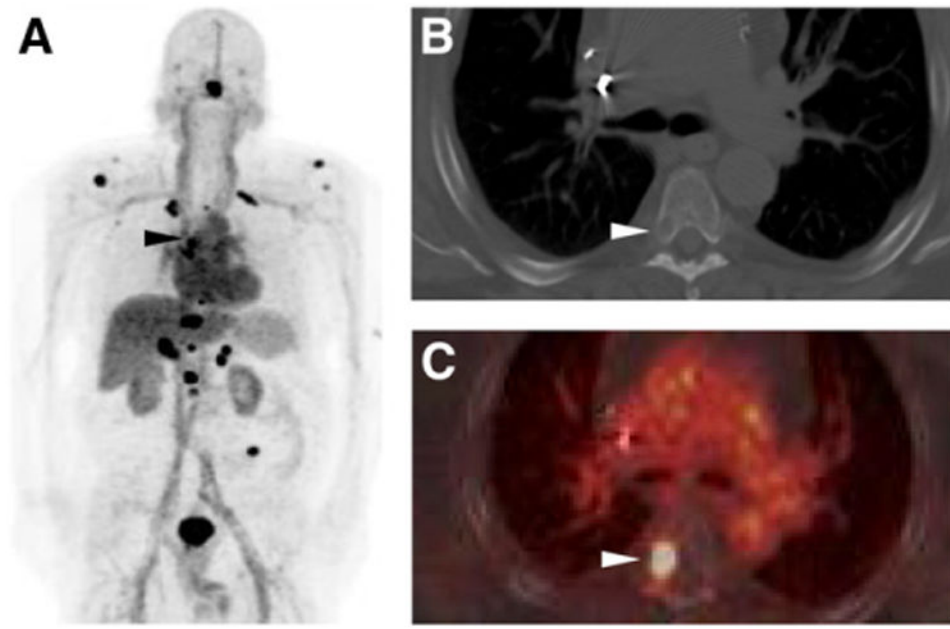
Figure 4.
^{18}F-DCFBC PET maximum-intensity projection (A), axial CECT (B), and axial fused ^{18}F-DCFBC PET/CT (C) images from patient with a subtle lytic bone lesion on CT that corresponded to intense ^{18}F-DCFBC uptake in right posterolateral T5 vertebral body and progressed on follow-up as patient's prostate-specific antigen level continued to rise (black and white arrowheads in A–C).
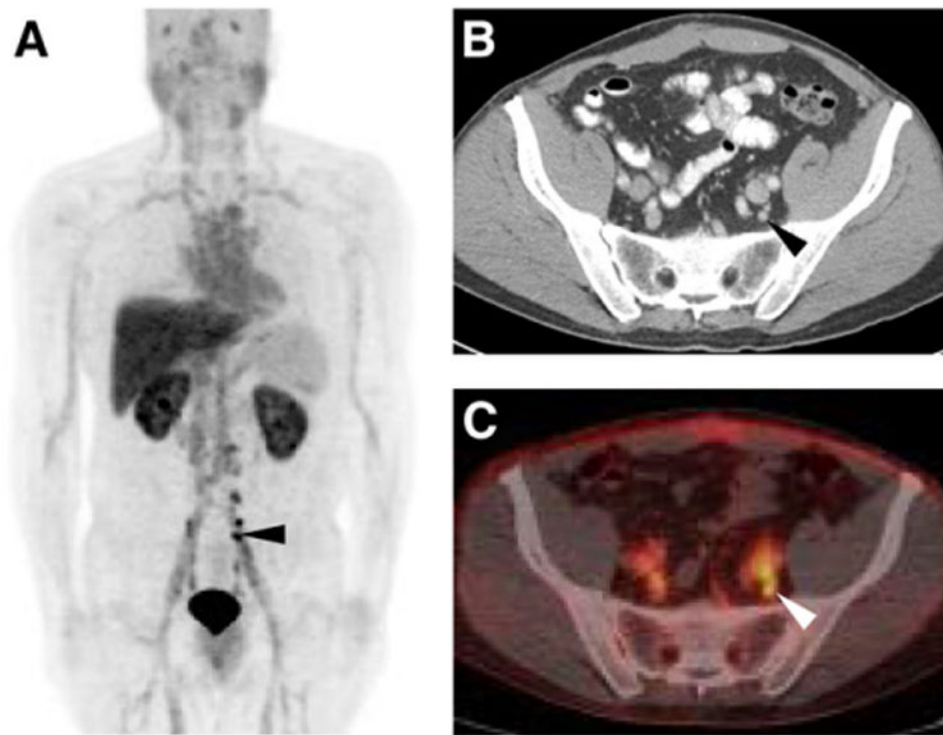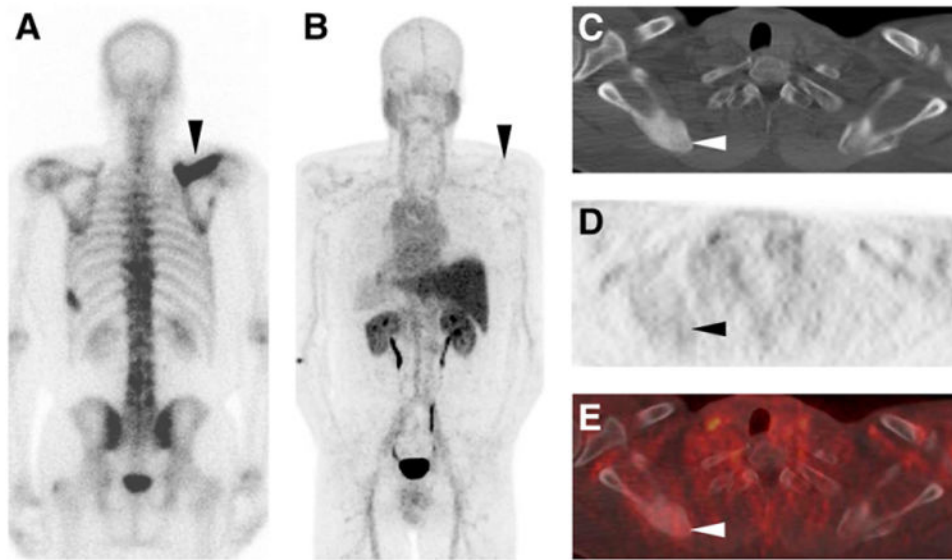
Figure 5.
^{18}F-DCFBC PET maximum-intensity projection (A), axial CECT (B), and axial fused ^{18}F-DCFBC PET/CT (C) images demonstrating intense ^{18}F-DCFBC uptake in multiple small pelvic lymph nodes that had been deemed too small to be definitively disease-involved on CECT (black and white arrowheads in A–C). Lymph nodes decreased in size on follow-up imaging and correlated with fall in patient's prostate-specific antigen level to undetectable.

Figure 6.
Posterior projection planar BS (A), ^{18}F-DCFBC PET maximum-intensity projection (posterior view, B), axial CT (C), axial ^{18}F-DCFBC PET (D), and axial fused ^{18}F-DCFBC PET/CT (E) images from patient who was postprostatectomy with rising prostate-specific antigen and was naïve to systemic androgen-deprivation therapy and chemotherapy. Imaging demonstrates intense ^{99m}Tc-MDP uptake on BS and corresponding dense sclerosis on CT of right scapula without significant ^{18}F-DCFBC uptake (black and white arrowheads in A–E). This lesion progressed in extent to involve more of scapula on follow-up imaging in correlation with rising prostate-specific antigen level in this patient.

Table 1

Selected Clinical and Demographic Data on Patients Imaged in This Study

Patient no.	Age (y)	Prostate-specific antigen (ng/mL)	Serum folate (ng/mL; normal, 2.5–20)	Red cell folate (ng/mL; normal, 160–855)	Testosterone (ng/dL)	Prior prostate cancer therapy
1	72	81.8	>24	478	<20	Prostatectomy, external-beam radiation to the pelvis, androgen deprivation
2	83	11.6	14.6	429	245	External-beam radiation to the pelvis
3	61	38.9	>24	559	<20	External-beam radiation to the pelvis, androgen deprivation
4	70	8.3	12	268	247	Prostatectomy
5	68	67.6	13.6	361	465	None
6	76	31.4	>24	627	<20	Prostatectomy, androgen deprivation
7	59	99.6	>24	433	<20	Androgen deprivation, docetaxel, external-beam radiation to the spine
8	69	95.8	18.1	486	<20	External-beam radiation to the pelvis, androgen deprivation
9	69	6.7	17.1	359	<20	Androgen deprivation
10	61	48.3	16.6	NA	331	Prostatectomy, external-beam radiation to the pelvis
11	73	98.8	>24	NA	280	Prostatectomy
12	62	564.5	11.8	NA	<20	Androgen deprivation, docetaxel, tasquinimod, external-beam radiation to the right hip, ^{223}Ra
13	55	62.1	10.3	NA	442	Prostatectomy
14	58	3.5	11.8	584	273	Prostatectomy, external-beam radiation to the pelvis
15	77	316.1	14.2	860	<20	Androgen deprivation, abiraterone
16	75	6.7	10.4	666	746	Prostate brachytherapy
17	75	83.6	22	1049	538	External-beam radiation to the pelvis

NA = not available.

Table 2

Estimated Proportion of Agreement in Metastatic Lesion Detection Between PET and CIM, Accounting for Intrapatient Clustering Effects by GEE Regression Model Analysis

Modality			All patients				HNPC patients				CRPC patients			
PET	CT	BS	All lesions	Lymph node lesions	Bone lesions	Visceral lesions	All lesions	Lymph node lesions	Bone lesions	Visceral lesions	All lesions	Lymph node lesions	Bone lesions	Visceral lesions
P	N/E	–	0.30 (0.17–0.48)	0.39 (0.21–0.62)	0.24 (0.11–0.46)	0.18 (0.06–0.42)	0.40 (0.20–0.65)	0.33 (0.08–0.73)	0.34 (0.12–0.67)	0.23 (0.07–0.56)	0.22 (0.10–0.42)	0.50 (0.45–0.54)	0.16 (0.05–0.42)	0.12 (0.02–0.49)
P	–	N/E	0.44 (0.28–0.61)	NA	0.22 (0.12–0.36)	NA	0.55 (0.32–0.76)	NA	0.28 (0.12–0.52)	NA	0.31 (0.14–0.57)	NA	0.18 (0.07–0.38)	NA
P	N/E*		0.44 (0.28–0.61)	0.90 (0.75–0.96)	0.22 (0.12–0.36)	0.41 (0.17–0.69)	0.55 (0.32–0.76)	0.84 (0.44–0.97)	0.28 (0.12–0.52)	0.39 (0.11–0.77)	0.31 (0.14–0.57)	0.93 (0.83–0.97)	0.18 (0.07–0.38)	0.42 (0.12–0.80)
N/E	P	–	0.07 (0.04–0.14)	0.07 (0.01–0.39)	0.09 (0.05–0.17)	0.05 (0.01–0.28)	0.06 (0.01–0.24)	0.17 (0.02–0.63)	0.07 (0.02–0.21)	0.00 (0.00–0.00)	0.08 (0.04–0.16)	0.00 (0.00–0.00)	0.10 (0.04–0.21)	0.08 (0.01–0.46)
N/E	–	P	0.03 (0.01–0.08)	NA	0.05 (0.02–0.12)	NA	0.03 (0.01–0.19)	NA	0.06 (0.01–0.29)	NA	0.03 (0.01–0.08)	NA	0.04 (0.02–0.11)	NA
N/E	P*		0.08 (0.04–0.16)	0.07 (0.01–0.39)	0.10 (0.06–0.18)	0.05 (0.01–0.28)	0.07 (0.01–0.27)	0.17 (0.02–0.63)	0.08 (0.02–0.27)	0.00 (0.00–0.00)	0.09 (0.05–0.17)	0.00 (0.00–0.00)	0.11 (0.06–0.21)	0.08 (0.01–0.46)

*
Combined CIM (CT and BS).

P = positive; N/E = negative/equivocal; NA = not applicable.

Data in parentheses are 95% CIs.

Table 3

List of Prostate Cancer Therapies Received by Patients in This Study in Follow-up Period After ^{18}F-DCFBC PET Imaging

Patient no.	Therapy after ^{18}F-DCFBC PET	Time to imaging follow-up	Follow-up imaging modalities available
1	Started sipuleucel-T	6 mo	Na[18]F PET/CT
2	Started androgen deprivation	4 mo	BS
3	Continued androgen deprivation	NA	NA
4	Started androgen deprivation	2 mo	CECT, BS
5	Started androgen deprivation	6 mo	CECT, BS
6	Started cabazitaxel	4 mo	CECT, BS
7	Entered hospice	NA	NA
8	Continued androgen deprivation	NA	NA
9	External-beam radiation to the pelvis, continued androgen deprivation	4 mo	CECT, BS
10	Started androgen deprivation	NA	NA
11	Started androgen deprivation	6 mo	CECT, BS
12	Continued [223]Ra	3 mo	CECT, BS
13	Started androgen deprivation	1y	PSMA PET/CT
14	External-beam radiation to pelvic lymph node, started nelfinavir	3 mo	CECT
15	Continued androgen deprivation, started veliparib	3 mo	CECT, BS
16	No follow-up information available	NA	NA
17	Started androgen deprivation	1 mo	CECT

Time to follow-up and available modalities at follow-up are also noted. Patient 13 underwent follow-up PET/CT imaging with PSMA-targeted radiotracer (^{18}F-DCFPyL) different from radiotracer primarily described here.

NA = not available.

Table 4

Sensitivity, with Equivocal Lesions Considered Either Positive or Negative for Metastases in 2 Separate Analyses, for ^{18}F-DCFBC PET and CIM as Estimated by GEE Regression Model Analysis

Modality	Sensitivity (equivocal lesions considered negative)	Sensitivity (equivocal lesions considered positive)
^{18}F-DCFBC PET	0.92 (0.80–0.97)	0.88 (0.70–0.96)
CECT	0.64 (0.41–0.82)	0.77 (0.58–0.89)
BS	0.40 (0.20–0.65)	0.43 (0.25–0.63)
CIM (BS and CECT)	0.71 (0.49–0.86)	0.82 (0.60–0.93)

Data in parentheses are 95% CIs.